npj Climate and Atmospheric Science https://doi.org/10.1038/s41612-026-01352-5

Article in Press

Enhanced NO_2-driven multiphase formation of particulate nitrate and sulfate under high-humidity conditions

Received: 10 October 2025

Accepted: 4 February 2026

Cite this article as: Lin, Z., Ji, X., Xu, L. *et al.* Enhanced NO_2-driven multiphase formation of particulate nitrate and sulfate under high-humidity conditions. *npj Clim Atmos Sci* (2026). https://doi.org/10.1038/s41612-026-01352-5

Ziyi Lin, Xiaoting Ji, Lingling Xu, Gaojie Chen, Chen Yang, Keran Zhang, Feng Zhang, Lingjun Li, Yuping Chen & Jinsheng Chen

Enhanced NO_2-driven multiphase formation of particulate nitrate and sulfate under high-humidity conditions

Ziyi Lin[1,2,3], Xiaoting Ji[1,2,3], Lingling Xu[1,2,3]*, Gaojie Chen[1,2,3], Chen Yang [1,2,3], Keran Zhang[1,2,3], Feng Zhang[1,2], Lingjun Li[1,2,3], Yuping Chen[1,2,3], Jinsheng Chen[1,2,3]*

[1]State Key Laboratory of Advanced Environmental Technology, Institute of Urban Environment, Chinese Academy of Sciences, Xiamen 361021, China
[2]Fujian Key Laboratory of Atmospheric Ozone Pollution Prevention, Institute of Urban Environment, Chinese Academy of Sciences, Xiamen 361021, China
[3]University of Chinese Academy of Sciences, Beijing 100049, China

*Correspondence to: jschen@iue.ac.cn (Jinsheng Chen); linglingxu@iue.ac.cn (Lingling Xu)

Abstract:

Fast atmospheric particulate nitrate and sulfate formation under high-humidity condition have been extensively observed; however, the underlying chemical mechanisms and their relative contributions remain poorly understood. This study examined the characteristic high-humidity events (HHEs) in southern China during spring, providing field observation evidence for the crucial role of NO_2-driven multiphase reactions in particulate nitrate and sulfate formation. Our findings revealed efficient nitrate formation during early HHEs, likely facilitated by enhanced NO_2 uptake via disproportionation reaction. As humidity increased and fog formed, S(IV) oxidation competitively consumed NO_2 and N(III), causing rapid sulfate formation. The resulting N(III), produced from the oxidation of S(IV) by NO_2 (aq), further oxidized S(IV) effectively in droplets due to its slow liquid-gas mass transfer rate. A state-of-the-art multiphase box model demonstrated that NO_2 uptake and SO_2 oxidation by NO_2/N(III) represent dominant formation pathways during HHEs, accounting for 45.4% and 63.6% of the total nitrate and sulfate production, respectively. These results highlight the critical importance of NO_2-driven multiphase chemistry in particulate pollution under high-humidity environments.

Introduction.

Despite the implementation of extensive air pollution control measures in China, particulate matter (PM) pollution remains a persistent environmental challenge[1, 2], significantly impacting atmospheric visibility, air quality, and human health. These pollution events are typically associated with stagnant meteorological conditions, high relative humidity, and rapid accumulation of secondary inorganic aerosols, particularly nitrate (NO_3^-) and sulfate (SO_4^{2-})[3, 4, 5, 6]. Under such high-humidity environments where atmospheric oxidant levels are generally suppressed, nitrogen dioxide (NO_2) has been regarded as an important species in the rapid production of these secondary inorganic species[7, 8, 9].

Traditional views suggested a small uptake coefficient of NO_2 on bulk water (around 10^{-7})[10], which led to the heterogeneous uptake of NO_2 being overlooked in many previous studies. However, aerosol water exists as highly concentrated aqueous solutions with higher ionic strength compared to bulk water[11]. Recent laboratory studies have revealed that elevated ionic strength could facilitate NO_2 uptake, making the reaction rate on aerosols one order of magnitude higher than that in bulk water[12]. Field studies also provided the evidence of enhanced NO_2 uptake on deliquesced aerosol and wet ground surfaces[13]. Nevertheless, most research have focused on HONO, another product of NO_2 disproportionation reaction, while neglecting its contribution to NO_3^-[9, 14, 15]. Similarly, the oxidation rate of dissolved SO_2 (S(IV) = $SO_2{\cdot}H_2O + HSO_3^- + SO_3^{2-}$) by NO_2 on acidic aerosols was found to be three orders of magnitude higher than that in bulk water[16]. It has also been observed that the oxidation of S(IV) by NO_2 contributed significantly to SO_4^{2-} formation in high-humidity haze events[6, 7]. In addition, nitrite ions (NO_2^-), a product of the S(IV) + NO_2 reaction, can serve as an oxidant to further convert S(IV) to SO_4^{2-}. However, whether the oxidation of S(IV) to SO_4^{2-} is mainly driven by NO_2 or by N(III) (≡ HONO (aq) + NO_2^-) remains controversial. On the one hand, field studies have indicated that the reaction rate between N(III) and S(IV) increased under high pH caused by rich-ammonia during the haze in northern China, leading to rapid SO_4 formation[2-8, 17]. On the other hand, laboratory and simulation studies have demonstrated that in acidic aerosols, N(III) tended to be released into the atmosphere as HONO, therefore the oxidation of S(IV) by N(III) could be negligible[18, 19]. Currently, the detailed processes and the role of NO_2 in the formation of NO_3^- and SO_4^{2-} in real high-humidity atmosphere are not fully understood.

Due to the influence of monsoons, high-humidity events (HHEs) frequently occur in southern China from February to April each year. These HHEs are typically associated with quasi-stationary fronts, formed by the convergence of warm, moist oceanic air masses from the ocean and cold, dry continental air masses[20]. Under such high-humidity weather systems, the atmosphere becomes well-mixed and extremely stagnant, creating conditions highly conducive to the formation of secondary inorganic aerosols like NO_3^- and SO_4^{2-}. This environment provides a unique opportunity to investigate aerosol formation mechanisms under realistic high-humidity conditions. In this work, we conducted multiparameter field observations in Xiamen, a coastal city in southern China, where quasi-stationary front frequently occurred. Based on observational data and the relationships among key species (e.g., NO_2, HONO, N_2O, NO_3^- and SO_4^{2-}), we found evidence for NO_2 uptake, and for the oxidation of S(IV) by NO_2 and N(III). Furthermore, we incorporated aqueous-phase and heterogeneous chemical mechanisms into a chemical box model to assess the contributions of different reactions to NO_3^- and SO_4^{2-} formation within multiphase systems during HHEs. This study highlights the significant role of previously overlooked NO_2-driven multiphase chemistry in secondary inorganic aerosol formation, elucidates its underlying causes, and enhances the understanding of PM pollution prediction in high-humidity atmosphere.

Results and discussion

Overview of field observations. Figure 1 shows the time series of chemical species and meteorological parameters at the supersite, located on the rooftop of an Institute of Urban Environment (IUE) building in Xiamen from March 2 to 18, 2024. During the observation period, two distinct HHEs (HHE1 and HHE2) were identified, occurring on March 3–6 and March 15–17, respectively. Both events exhibited characteristic meteorological parameters indicative of elevated relative humidity (mean RH = 71.3% and 81.2%), suppressed ultraviolet radiation (UV = 11.1 and 14.0 W/m^2), and highly stable atmospheric conditions including low wind speeds (WS = 0.92 and 0.56 m/s) and shallow boundary layer heights (BLH = 274 and 260 m). As illustrated in Supplementary Figure 1, both events were affected by quasi-stationary fronts. Specifically, the first front developed in southern China on March 3, driven by the confrontation of an oceanic air mass and an inland air mass from central China. The front reached its peak intensity on March 5, and dissipated on March 6 as the inland cold air mass strengthened and precipitation occurred. The second front evolved similarly, beginning on March 15, peaking on March 17, and ending on March 18. The frontal position indicated that the quasi-stationary front during HHE1 approached closer to the observation site than during HHE2.

During both HHEs, RH increased rapidly and visibility deteriorated seriously, accompanied by warm air advection and the eventual formation of fog in the later stage. $PM_{2.5}$ concentrations rose significantly, with a mean value of 49.9 μg/m^3 (maximum value was 96.0 μg/m^3), exceeding those during non-HHE periods (normal periods, 34.9 μg/m^3). Notably, chemical speciation revealed two distinct stages of secondary inorganic aerosol formation within HHEs. In the early stage (ES-HHE), NO_3^- dominated the water-soluble inorganic ions (WSII) in $PM_{2.5}$, accounting for an average of 47.8% of the total WSII mass. In the later stage (LS-HHE), SO_4^{2-} concentrations surged, even surpassing NO_3^- levels during LS-HHE1, and contributed on average value of 38.8% to WSII. From a precursor perspective, although NO_3^- increased concurrently with rising NO_2 during ES-HHE1 and SO_4^{2-} increased with consumed SO_2 during LS-HHE2, this pattern was not consistent across both HHEs. The observations suggest that the transition from NO_3^- to SO_4^{2-} dominance cannot be attributed solely to precursor variations, but rather points to their formation mechanisms as the HHE progressed. As shown in Figure 1 and Supplementary Figure 2, the mean concentrations of O_3, HONO, and NO_2 during HHEs were 12.8, 3.0, and 30.0 ppb, while 28.0, 1.5, and 21.0 ppb during normal periods. Compared to the normal periods and previous studies[21, 22, 23], the atmospheric environment during HHEs was characterized by depleted O_3 production and elevated levels of nitrogen species (NO_2 and HONO). This aligns with those reported in Beijing and the North China Plain (NCP), where reactive nitrogen chemistry in aerosol water has been identified as a key contributor to sulfate and $PM_{2.5}$ formation during haze events[7, 8]. Therefore, we further examined the role of nitrogen chemistry in NO_3^- and SO_4^{2-} production during HHEs. Above analysis indicates that HHEs in southern China share similar characteristics. Given the closer proximity of the quasi-stationary front to the monitoring site during HHE1, this event was selected as a representative case for subsequent mechanistic analysis.

Evidence for NO_2-driven NO_3^- and SO_4^{2-} formation. The initial phase of the HHE period was characterized by a pronounced accumulation of NO_3^-. Traditional chemical pathways for NO_3^- formation mainly include daytime gas-phase oxidation of NO_2 by OH radicals and nocturnal heterogeneous uptake of dinitrogen pentoxide (N_2O_5)[24]. However, under the low-O_3 conditions during HHE, the oxidation of NO_2 to N_2O_5 and subsequent heterogeneous N_2O_5 hydrolysis would be weakened. The product of NO_2 concentration, aerosol liquid water content (ALWC), and aerosol surface area (SA) was used as a proxy to reflect the heterogeneous reaction capability of NO_2[13, 25, 26]. As shown in Figure 2a, elevated values of $NO_2\times ALWC\times SA$ were observed during HHE (represented by HHE1, the same below) relative to normal periods. The correlation between $NO_2\times ALWC\times SA$ and NO_3^- was strong during ES-HHE (r = 0.78, $p < 0.05$) but weak during LS-HHE (r = 0.48, $p < 0.05$). This suggests that heterogeneous reactions played a more important role in NO_3^- formation during the ES-HHE period. Supplementary Table S1 further indicates that within the proxy, both NO_2 concentrations and SA levels were significantly higher during ES-HHE. This condition facilitated more frequent contact between NO_2 molecules and particle surfaces, thereby promoting the heterogeneous formation of NO_3^-. In contrast, during the LS-HHE period, only ALWC showed a significant increase, which alone was insufficient to enhance the heterogeneous conversion of NO_2 to NO_3^-. The difference between the two stages might also be related to halogen ions from sea salt. Previous studies have indicated that the sea-salt halogens would promote the interaction between NO_2 and aerosol/ground surfaces via electric field attraction[18, 27, 28], or form $[X\text{-}NO_2]^-$ intermediates (X = Cl^-, Br^-, I^-)[29], thereby enhancing NO_2 uptake on surfaces. Supplementary Figure 3 shows a strong correlation between Na^+ and Cl^- during ES-HHE, confirming the influence of sea salt aerosols transported by marine air masses. Interestingly, a notable increase in HONO concentrations was observed concurrently with NO_3^- during the HHE period (Figure 1). Vehicle exhaust emissions are important sources for HONO in Xiamen[21], while they could not explain the abnormal rise of HONO during HHE as no synchronous rise of NO_2 was observed, suggesting the existence of additional HONO sources. Previous studies[30, 31] have demonstrated that the disproportionation reaction of NO_2 simultaneously generates nitric acid and HONO (reaction 1) and this reaction can occur in aerosols and on acidic surfaces. Figure 2 shows the relationship between HONO and NO_3^-/SO_4^{2-} during nighttime only, to avoid interference from NO + OH formation and rapid HONO photolysis during the day. As illustrated in Figure 2b, HONO and NO_3^- exhibited a strong positive correlation (r = 0.92 and r = 0.78 in ES-HHE and LS-HHE respectively), suggesting a possible contribution of NO_2 uptake and disproportionation to HONO production. Notably, the NO_3^-/HONO slope during ES-HHE (1.27 ppb/ppb) was close to the 1:1 stoichiometric ratio, in contrast to the lower ratio in LS-HHE (0.61 ppb/ppb). This alignment implies that NO_2 disproportionation was likely the major source for nighttime NO_3^- during the ES-HHE period. Additionally, although elevated SO_2 levels during ES-HHE1 could also increase HONO via reaction 2, the HONO budget derived from a box model (Supplementary Figure 9) indicates that the contribution of this pathway was relatively minor.

$$2NO_2 + H_2O_{(ad)} + \text{aerosol/ground surface} \rightarrow HNO_{3(ad)} + HONO \quad (1)$$

The later stage of HHE exhibited a predominance of SO_4^{2-} in $PM_{2.5}$. Figure 2c shows that SO_4^{2-} had strong positive correlations with the product of NO_2 concentration and ALWC in both ES-HHE and LS-HHE. Notably, the slope of SO_4^{2-} versus $NO_2\times ALWC$ during LS-HHE was an order of magnitude higher than that during ES-HHE, indicating enhanced NO_2-driven aqueous chemical processes contributing to SO_4^{2-} formation during LS-HHE. Supplementary Table S1 further shows a substantially increase in ALWC during LS-HHE, thereby creating more favorable conditions for NO_2-involved aqueous-phase reactions. As shown in reactions 2–5, the oxidation of S(IV) by $NO_2(aq)$ can simultaneously generate SO_4^{2-} and N(III). N(III) maintains gas-liquid equilibrium with HONO, which tends to be released into the atmosphere as HONO in acidic aerosol water[18, 19]. Figure 2d shows a significantly enhanced positive correlation between SO_4^{2-} and nocturnal HONO during ES-HHE (r = 0.68, $p < 0.05$), distinguishing from the normal and LS-HHE periods. This implies that the aqueous oxidation of S(IV) by NO_2 likely contributed to both SO_4^{2-} and HONO simultaneously during ES-HHE. Similarly, halogen ions from sea salt could also facilitate the uptake of NO_2 at the aqueous interface, promoting its subsequent aqueous-phase reactions[19, 32, 33]. In contrast, the correlation between HONO and SO_4^{2-} became negative in LS-HHE, implying different SO_4^{2-} formation mechanisms in LS-HHE. Previous studies demonstrated that

N(III) maintains equilibrium with HONO and can also oxidize S(IV) to form S(VI) and N_2O[34, 35]. As respective products of reaction 2 and reaction 5 pathways, HONO and N_2O may indicate their relative importance. Supplementary Figure 4 illustrates a lower slope of HONO versus N_2O during LS-HHE (0.29 ppb/ppb) is lower than during ES-HHE (0.38 ppb/ppb), suggesting increased importance of aqueous-phase N(III) to S(IV) oxidation during LS-HHE. The shift of N(III) effect was likely associated with RH variations. During the LS-HHE period, fog occurred, and some studies have suggested that fog droplets could provide an effective medium for aqueous-phase oxidation of S(IV) by N(III)[36, 37]. Therefore, we hypothesize that during LS-HHE, HONO produced from S(IV) oxidation through reaction 2 could further effectively oxidize S(VI) via reaction 5, which will be further verified in the subsequent modeling analysis.

$$S(IV) + 2NO_2(aq) + H_2O \rightarrow S(VI) + 2H^+ + 2NO_2^- \quad (2)$$

$$HNO_2(aq) \rightleftharpoons H^+ + NO_2^- \quad (3)$$

$$HONO \rightleftharpoons HNO_2(aq) \quad (4)$$

$$2S(IV) + N(III) \rightarrow N_2O + 2S(VI) + \text{other products} \quad (5)$$

Multiphase chemical box model elucidates NO_2-driven mechanisms. The above correlations analysis suggests that NO_2-driven multiphase chemical processes could explain the observed increases in NO_3^- and SO_4^{2-} concentrations. As these NO_2-driven reactions were influenced by multiple meteorological factors and competing atmospheric reaction pathways, we developed a comprehensive multiphase box model to assess the role of NO_2-driven chemistry during HHEs (See Methods for full implementation details). This model incorporated aerosol gas-aqueous equilibrium processes, unified gas-aqueous phase chemical parameters, and detailed heterogeneous as well as aqueous-phase reaction mechanisms. The model demonstrated good performance in simulating secondary inorganic aerosol formation (Fig. 3a–b), with r values increasing from 0.27 to 0.77 for NO_3^- and from statistically insignificant to 0.78 for SO_4^{2-}. These results supported the observational findings that NO_2 uptake, oxidation of S(IV) by $NO_2(aq)$, and oxidation of S(IV) by N(III) played crucial roles in NO_3^- and SO_4^{2-} formation during HHEs.

The average diurnal budget of NO_3^- and SO_4^{2-} during the HHE period and normal periods are summarized in Figure 3c-3d. During HHE period, the heterogeneous uptake of NO_2 contributed 45.4% to nitrate formation (Figure 3c). At nighttime (18:00–06:00), the contribution of NO_2 uptake reached 71.3%. This high contribution contrasted with previous studies in urban areas in China[38, 39, 40], which typically identified N_2O_5 uptake as the dominant nocturnal nitrate formation pathway. Figure 3e further shows the formation rates of NO_3^- and SO_4^{2-} via different reaction mechanisms across different periods. The mean NO_3^- production rate via NO_2 uptake was 2.90 μg/m^3/h during ES-HHE, significantly higher than those during LS-HHE (1.01 μg/m^3/h) and normal periods (0.68 μg/m^3/h). This supports our earlier inference that enhanced NO_2 uptake via disproportionation reactions predominantly contributed to the rapid formation of NO_3^- during the ES-HHE period. The model also captured the promotion of SO_4^{2-} formation by NO_2-driven mechanisms (Figure 3d). Acting as major oxidants, NO_2 and N(III) together contributed 63.6% to total sulfate production during the HHE period. A recent global modeling study reported that NO_3^- photolysis promotes sulfate formation via indirect renoxification pathways[19]. This effect was not reproduced in our model (Supplementary Figure 9), primarily because the lower radiation levels during our observation period were less favorable to photolytic reactions. As illustrated in Figure 3e, the aqueous-phase S(IV) oxidation rates directly by NO_2 were 0.87 and 0.98 μg/m^3/h during ES-HHE and LS-HHE, respectively, representing near 2.0-fold and 2.2-fold increases compared to normal periods (0.45 μg/m^3/h). The oxidation of S(IV) by NO_2 is pH-dependent. Although aerosol pH remained generally low during HHEs, we observed significantly elevated NH_3 concentrations (Supplementary Figure 6), comparable to levels reported during haze episodes in northern China[41]. These higher NH_3 levels would have effectively neutralized aerosol acidity, thereby promoting the heterogeneous oxidation of SO_2 by NO_2[42]. Notably, S(IV) oxidation by aqueous-phase N(III), which was negligible during ES-HHE and normal periods, became highly significant during LS-HHE, with a production rate of 0.46 μg/m^3/h. These findings indicate that N(III) effect was an important reason for the rapid increase in SO_4^{2-} observed in LS-HHE.

Figure 4b elucidates the factors responsible for the difference in S(IV) oxidation rates by N(III) between ES-HHE and LS-HHE. As described in the "Methods" section, the liquid-to-gas transfer rate (k_t) reflects the residence time of ions in the aqueous phase. For N(III), the transfer rate ($k_{t,N(III)}$) from the aerosol water to gaseous HONO exhibited an inverse relationship with aerosol radius, indicating slower release from larger aerosols. When H^+ concentrations below 10^{-3} mol/L, $k_{t,N(III)}$ correlated positively with [H^+], demonstrating that higher pH (lower [H^+]) promoted N(III) retention in the aqueous phase. During the observation period, the average aerosol radius measured by SMPS was 3.13×10^{-6} cm (see particle size spectra in Supplementary Figure 7), comparable to the value used in GEOS-Chem model[19], and the average aerosol pH derived from the ISORROPIA-II model was 2.49. These conditions could result in elevated $k_{t,N(III)}$ values, facilitating N(III) transfer to the atmosphere and consequently limiting S(IV) oxidation by N(III) prior to fog formation. In contrast, the radius of fog droplets in Chinese urban areas typically ranged from 2.0×10^{-4} to 7.5×10^{-4} cm[36, 43, 44], here we adopted 2.5×10^{-4} cm as a representative value. Meanwhile, within the documented fog water pH range of 4.7 to 6.9[6, 36, 43, 45], we assigned a fog pH of 6.43 based on precipitation samples measurements (see Methods). Thus, for fog droplets, the larger radius and higher pH both prolonged the residence time of N(III) in the aqueous phase, even at the lower limits of these parameters. Aside from $k_{t,N(III)}$, aerosol-water pH itself also positively influenced the S(IV) + N(III) reaction rate within typical aerosol pH ranges[8, 34]. The simulated isopleths of S(VI) formation indicated that, compared to aerosol conditions (Figure 4b, triangle symbol), the lower $k_{t,N(III)}$ and higher pH of fog droplets (pentagram symbol) synergistically enhanced the S(IV) + N(III) reaction rates, with notable sensitivity to $k_{t,N(III)}$ variations. These results demonstrate that fog in LS-HHE provided an optimized medium for the N(III) + S(IV) reaction, further highlighting the oxidative role of N(III) in SO_4^{2-} production under high-humidity conditions.

Conclusion and implication. In summary, we provide observational evidence and quantitative results demonstrating the significant role of NO_2-driven multiphase chemistry in NO_3^- and SO_4^{2-} formation during high-humidity events. HHEs were typically characterized by high humidity and stagnant meteorological conditions, which favored heterogeneous/aqueous phase reactions. Model simulations revealed that, compared to normal periods, NO_2-driven multiphase oxidation increased the formation rates of NO_3^- and SO_4^{2-} by an average of 1.54 μg/m^3/h and 0.63 μg/m^3/h, respectively. Figure 4 summarizes the proposed mechanisms. The ES-HHE was marked by a pronounced increase in NO_3^- concentration, during which NO_2 uptake (2.90 μg/m^3/h) exceeded N_2O_5 uptake, emerging as the dominant pathway for nocturnal NO_3^- formation. This enhanced NO_2 uptake was likely related to the influence of halogen ions transported by marine air masses during ES-HHE. As RH further increased with fog formation in LS-HHE, S(IV) oxidation competitively consumed NO_2 and N(III). While the aqueous-phase oxidation rate of S(IV) by NO_2 increased slightly from 0.87 μg/m^3/h in ES-HHE to 0.98 μg/m^3/h in LS-HHE, the contribution of N(III) to S(IV) oxidation became highly significant (0.46 μg/m^3/h) in LS-HHE compared to negligible levels in ES-HHE. This shift mainly arose from the higher pH and larger radius in fog droplets, which prolong the residence time of N(III) in aerosol water and enhance its reaction with S(IV), thereby leading to rapid SO_4^{2-} formation during LS-HHE. The NO_2-promoted oxidation of SO_2 to SO_4^{2-} under high humidity conditions has been widely reported in northern China, such as Beijing and the NCP[7, 8]. Our study demonstrates that this process also occurs in southern China despite distinct environmental conditions, such as more acidic aerosols and higher temperature. Figure 4c illustrates the detailed mechanisms during HHE, underscoring the enhanced role of NO_2-driven multiphase oxidation in secondary inorganic aerosol formation under high humidity conditions.

Despite significant reductions in SO_2 and NO_x emissions in China, sulfate and nitrate aerosols have decreased non-linearly relative to their precursors[2]. This phenomenon is likely associated with enhanced secondary transformation in the atmosphere, among which NO_2-driven multiphase oxidation under high-humidity conditions represents one such process. Furthermore, we observed substantial HONO (peaking near 8 ppb) produced from NO_2-driven multiphase reactions, including NO_2 disproportionation and direct SO_2 oxidation by NO_2. Since HONO photolysis is a major source of atmospheric OH radicals, this process may further contribute to the formation of secondary pollutants, such as secondary organic aerosols (SOA)[46]. Therefore, the overall influence of NO_2-driven multiphase chemistry on PM pollution requires further clarification. Although the multiphase model used here reproduced the observed variations in NO_3^- and SO_4^{2-} during HHEs, laboratory- and field-derived kinetic parameters remain essential to fully elucidate NO_2-driven chemistry on aerosol, ground and fog droplet surfaces. These parameters include, but are not limited to, kinetic data for NO_2 disproportionation, uptake coefficients on various aerosol types[12, 47, 48], and comprehensive physicochemical properties of fog droplet[49, 50]. Moreover, developing sophisticated models that couple broader atmospheric physical and chemical processes would improve the simulations of NO_3^- and SO_4^{2-} concentrations. Such efforts will enable more accurate assessments of NO_2-driven multiphase oxidation contributions to secondary aerosol formation, providing a scientific basis for predicting and mitigating PM pollution in high-humidity environments. For example, a clearer understanding of the threshold level of NO_2 could guide targeted NO*x* emission-reduction strategies, thereby aiding the effective prevention of PM pollution.

Methods

Field campaign. The field campaign was conducted at the Atmospheric Observation Supersite of the IUE, Chinese Academy of Sciences (24.61°N, 118.06°E) in Xiamen, China from March 2 to 18 of 2024. This site is surrounded by roads, office buildings, and residential apartments, representing a typical urban environment. Measurements were conducted approximately 70 meters above ground level and a detailed site description can be found elsewhere[22, 51]. All collected data were averaged into hourly values.

Detailed measurements of particulate matter, trace gases, and meteorological parameters were conducted during the campaign. The particulate-related parameters including $PM_{2.5}$, WSII (SO_4^{2-}, NO_3^-, NH_4^+, Cl^-, Na^+, Ca^{2+}, K^+, Mg^{2+}), particle size distribution (7–300 nm), and aerosol liquid water content (ALWC), were measured by a Thermo 1405DF (Thermo Fisher Scientific, Waltham, MA, USA), a MARGA ADI 2080 (Metrohm Applikon, Switzerland), a nano scanning mobility particle sizer (SMPS) (TSI, USA), and an aerosol hygroscopicity analyzer (PB-FRH100, BMET, Beijing, China), respectively. Trace gases (O_3, SO_2, CO) were monitored by Thermo models 49*i*, 43*i* and 48*i*. Nitrogen species including NO*x*, HONO, N_2O were measured by a Thermo 17*i*, a water-based long-path absorption photometer (WLPAP, Zhichen, Beijing, China), and an N_2O analyzer (HPGA-4301, Juguang, Hangzhou, China), respectively. Meteorological parameters (T, RH, P, UV, and wind speed) were recorded with an integrated sensor (150WX, Airmar, USA). Visibility was measured by a visibility sensor (Model 6400, Belfort, USA), while photolysis frequencies (JO^1D, JNO_2, JHONO, JNO_3, JHCHO and JH_2O_2) were determined using a photolysis spectrometer (FPS-100, Focused Photonics Inc., Hangzhou, China). Additionally, approximately 116 VOCs were analyzed by a gas chromatography-mass spectrometer (GC-FID/MS, Agilent 7890B/6977, China).

In addition, the pH of precipitation samples was monitored at a nearby station. Hourly BLH, horizontal wind speed, vertical wind speed, and 2-meter air temperature data were obtained from the ERA5 dataset[52].

Simulation of the ISORROPIA-II model. The ISORROPIA II model[53] was used to calculate the aerosol pH and ionic strength (I, mol/L). Model input included the concentrations of WSII in $PM_{2.5}$, RH and T. The simulation was performed in forward mode under metastable state conditions. The model results were validated by comparing simulated concentrations of major water-soluble inorganic ions with observations (Supplementary Figure 8). The pH and I were calculated as follows:

$$pH = -\log_{10}\frac{1000H^{+}_{air}}{ALWC} \tag{6}$$

where H^{+}_{air} is the concentration of particle hydronium (μg/m^3).

$$I = \frac{1}{2}\sum_{i=0}^{n} b_i z_i^2 \tag{7}$$

where b_i and z_i represent the molality (mol/kg) and charge of the i^{th} ion, respectively. The calculated pH and I were used as inputs for the multiphase box model simulations.

Construction of the multiphase box model. The multiphase box model was developed based on the Framework for 0-D Atmospheric Modeling (F0AM)[54] in a MATLAB-based platform, which has been widely used in previous field studies[55, 56] The base model adopted the gas-phase chemical mechanisms of Master Chemical Mechanism 3.3.1 (MCM v3.3.1 https://mcm.york.ac.uk/MCM/).

The multiphase box model was constructed by adding gas-aqueous equilibrium in aerosols, unifying units between gas-phase and aqueous-phase chemistry, and incorporating detailed heterogeneous and aqueous-phase chemical mechanisms.

To construct gas-aqueous equilibrium in the model, we considered gas-phase dissolution, aqueous-phase volatilization, and mass transport limitation. Gas dissolution follows Henry's law (see Supplementary Text S1for details):

$$[X(aq)] = P_{X(g)} \times H_{XT} \tag{8}$$

where X(aq) is the aqueous-phase concentration of species X (mol/L); $P_{X(g)}$ is the partial pressure of X (atm); and H_x is the Herny's law constant (mol/L/atm) at temperature T (K) which follows the van't Hoff equation:

$$H_{XT} = H_{XT_{298K}} \exp\left[-\frac{\Delta H_{298K}}{R}\left(\frac{1}{T}-\frac{1}{T_0}\right)\right] \tag{9}$$

For aerosol particles assumed to be spherical, the transfer rate(k_t) of an aqueous-phase species (Supplementary Text S2) to gas phase is parameterized as the volatilization rate[26]:

$$k_t = \left[\frac{1}{15}\frac{a^2}{D_{a,X}} + H_{XT}RT\left(\frac{a^2}{3D_{g,X}} + \frac{4a}{3c_X\alpha_X}\right)\right]^{-1} \tag{10}$$

where a is the aerosol/droplet radius (cm); $D_{a,X}$ is the aqueous-phase diffusion coefficient of X(aq) (cm^2/s); $D_{g,X}$ is the gas-phase diffusion coefficient of X(cm^2/s); c_X is the mean molecular velocity of X (cm/s); and α_X is mass accommodation coefficient of X. The loss of X(aq) due to transfer to the gas phase is described by:

$$\frac{d[X(aq)]}{dt} = [X(aq)] \times k_t \tag{11}$$

Since mass transport effects occur at the gas-aqueous interface, their kinetics parameterized as described in Supplementary Text S3. The mass transport coefficient (K_{MTX}) is determined by[57]:

$$K_{MTX} = \left[\frac{a^2}{3D_{g,X}} + \frac{4a}{3v_X\alpha_X}\right]^{-1} \tag{12}$$

To incorporate aqueous-phase chemistry into the gas-phase based model, we used the method as Jacob[58], converting the concentration of aqueous-phase species and the rate constants of aqueous-phase reactions to units consistent with gas-phase chemistry. The transformation as:

$$[X_i] = 6.023 \times 10^{20} LWC \times [X(aq)] \tag{13}$$

where X_i (molec/cm^3) is the format of Xaq in the multiphase box model and LWC is the liquid water content.

Supplementary Text S4 describes the chemical mechanisms incorporated into the model. Briefly, the heterogeneous mechanisms include NO_2 uptake, HNO_3 partitioning (formed from OH and NO_2 reactions), N_2O_5 uptake, nitrate photolysis, and SO_2 uptake. As reaction rates in high-ionic-strength aerosols differ from those in dilute solutions[6, 12], the effect of ionic strength on NO_2 uptake coefficient was considered. Given the high-RH simulation environment, RH-enhanced rates of NO_2 uptake, RH-dependent coefficients of N_2O_5 uptake, and RH-dependent coefficients of SO_2 uptake were incorporated. In addition, the effects of pH on gas-particle partitioning were taken into account. Nitrate formation via the gas-phase OH + NO_2 reactions was adjusted by the partitioning ratio of $NO_3^-/(NO_3^-+HNO_3)$, which was simulated by the ISORROPIA-II model with a mean value of 0.81. Aqueous-phase S(IV) oxidation reactions mainly involve five classic oxidants: NO_2, O_3, N(III), hydrogen peroxide (H_2O_2), and transition metal ions (TMI)[59]. Organic oxidants for S(IV) including HCHO and hydroxymethyl hydroperoxide (HMHP) were also considered[60, 61, 62]. Aqueous chemistry occurring in fog droplets follows the same mechanisms as for aerosols. Detailed reaction rates and kinetic expressions are summarized in Supplementary Table 2 and Table 3. A detailed budget analysis of HONO is provided in Supplementary Text S4.3 and its simulated budget is shown in Supplementary Figure 9.

Setup of the multiphase box model.

Measured hourly data of trace gases (O_3, NO, NO_2, CO, SO_2, HONO, HCHO, and VOCs,), meteorological variables (T, RH, P, BLH, and photolysis frequencies), and WSII (SO_4^{2-} and NO_3^-), were used to constrain the multiphase box model. A 3-day spin-up was set prior to each simulation to stabilize the concentrations of intermediate species. In addition to chemical processes, physical loss processes including dry deposition and dilution were considered. The dry deposition velocities for the constrained species were set according to Liu et al[22]. The basic dilution rate was set to 2×10^{-5} s^{-1}, varying with boundary layer height. For all simulation periods, the aerosol radius and aerosol pH were set to the mean geometric radius measured by SMPS (Supplementary Figure 7) and the results of the ISORROPIA II model (Supplementary Figure 2a), respectively. During the ES-HHE and normal periods, in the absence of fog, the droplet radius was set to 0, which means that aqueous-phase chemical processes on the droplets would not occur. During the LS-HHE period, the droplet radius was set to 2.5×10^{-4} cm based on a previous modelling study[36], and the droplet pH was assigned a value of 6.43 according to March precipitation sample measurements (Supplementary Table 5).

To identify the relationships between $k_{t,N(III)}$ and relevant parameters (aerosol radius, H^+ concentrations), the mean diurnal profiles during HHE-1 were used as a base for further scenario simulations. Different aerosol radii (from 10^{-7} cm to 10^1 cm) and H^+ concentrations (from 10^{-8} mol/L to 10^{-1} mol/L) were tested in various calculation scenarios to explore their relationships with $k_{t,N(III)}$. Furthermore, a series of simulations with varying $k_{t,N(III)}$ and $[H^+]$ were conducted to examine the response of the S(IV) oxidation rate by N(III) to changes in both parameters.

Data availability

Observed data and data analysis methods are available on request from Jinsheng Chen (jschen@iue.ac.cn).

Acknowledgements

This work was funded by the National Natural Science Foundation of China (U22A20578), the guiding project of seizing the commanding heights of "self-purifying city" (IUE-CERAE-202402), the National Key Research and Development Program (2022YFC3700304), STS Plan Supporting Project of the Chinese Academy of Sciences in Fujian Province (2023T3013), and Xiamen Atmospheric Environment Observation and Research Station of Fujian Province.

Author contributions:

Z.L. contributed to the methodology, data curation, software, analysis and writing of the original draft. L.X., and J.C. contributed to the conceptualization, investigation, data curation, reviewing and editing the text, supervision, and funding acquisition X.T., G.C., C.Y., K.Z., F.Z., L.L., and Y.C. provided useful advice and revised the manuscript.

Competing interests

The authors declare no competing financial or non-financial interests.

References:

1. Zhai S*, et al.* Control of particulate nitrate air pollution in China. *Nature Geoscience.* **14**, 389-395 (2021).

2. Zhao Y*, et al.* Decline in bulk deposition of air pollutants in China lags behind reductions in emissions. *Nature Geoscience.* **15**, 190-195 (2022).

3. Wu X*, et al.* The characteristics of air pollution induced by the quasi-stationary front: Formation processes and influencing factors. *Science of The Total Environment.* **707**, 136194 (2020).

4. Cheng C*, et al.* The significant contribution of nitrate to a severe haze event in the winter of Guangzhou, China. *Science of The Total Environment.* **909**, 168582 (2024).

5. Li H*, et al.* Nitrate-driven urban haze pollution during summertime over the North China Plain. *Atmos Chem Phys.* **18**, 5293-5306 (2018).

6. Wang G*, et al.* Persistent sulfate formation from London Fog to Chinese haze. *Proceedings of the National Academy of Sciences.* **113**, 13630-13635 (2016).

7. Cheng Y*, et al.* Reactive nitrogen chemistry in aerosol water as a source of sulfate during haze events in China. *Science Advances.* **2**, e1601530 (2016).

8. Wang J*, et al.* Fast sulfate formation from oxidation of SO_2 by NO_2 and HONO observed in Beijing haze. *Nature Communications.* **11**, 2844 (2020).

9. Xu W*, et al.* Efficient Nitrate Formation in Fog Events Implicates Fog Interstitial Aerosols as Significant Drivers of Atmospheric Chemistry. *Environmental Science & Technology.* **58**, 22298-22311 (2024).

10. Lee YN, Schwartz SE. Reaction kinetics of nitrogen dioxide with liquid water at low partial pressure. *The Journal of Physical Chemistry.* **85**, 840-848 (1981).

11. Cheng Y, Su H, Koop T, Mikhailov E, Pöschl U. Size dependence of phase transitions in aerosol nanoparticles. *Nature Communications.* **6**, 5923 (2015).

12. Gen M*, et al.* Rapid hydrolysis of NO_2 at High Ionic Strengths of Deliquesced Aerosol Particles. *Environmental Science & Technology.* **58**, 7904-7915 (2024).

13. Stutz J*, et al.* Relative humidity dependence of HONO chemistry in urban areas. *Journal of Geophysical Research: Atmospheres.* **109**, (2004).

14. Zhang X*, et al.* Elucidating HONO formation mechanism and its essential contribution to OH during haze events. *npj Climate and Atmospheric Science.* **6**, 55 (2023).

15. Xuan H*, et al.* Relative humidity driven nocturnal HONO formation mechanism in autumn haze events of Beijing. *npj Climate and Atmospheric Science.* **7**, 193 (2024).

16. Liu T, Abbatt JPD. Oxidation of sulfur dioxide by nitrogen dioxide accelerated at the interface of deliquesced aerosol particles. *Nature Chemistry.* **13**, 1173-1177 (2021).

17. Li L, Hoffmann MR, Colussi AJ. Role of Nitrogen Dioxide in the Production of Sulfate during Chinese Haze-Aerosol Episodes. *Environmental Science & Technology.* **52**, 2686-2693 (2018).

18. Wang G*, et al.* Atmospheric sulfate aerosol formation enhanced by interfacial anions. *PNAS Nexus.* **4**, (2025).

19. Liu L*, et al.* Global Impact of Particulate Nitrate Photolysis on Fine Sulfate Aerosol. *Environmental Science & Technology Letters.* **11**, 961-967 (2024).

20. Cho J-H, Kim H-S. Influence of Aqueous-Phase Chemistry on the Concentrations of $PM_{2.5}$ and Hydrometers During the Development of Convective Clouds Over the Yellow Sea in July of 2017. *Journal of Geophysical Research: Atmospheres.* **129**,

e2023JD039421 (2024).
21. Hu B, *et al.* Exploration of the atmospheric chemistry of nitrous acid in a coastal city of southeastern China: results from measurements across four seasons. *Atmos Chem Phys.* **22**, 371-393 (2022).
22. Liu T, *et al.* Atmospheric oxidation capacity and ozone pollution mechanism in a coastal city of southeastern China: analysis of a typical photochemical episode by an observation-based model. *Atmos Chem Phys.* **22**, 2173-2190 (2022).
23. Chen G, *et al.* Increasing Contribution of Chlorine Chemistry to Wintertime Ozone Formation Promoted by Enhanced Nitrogen Chemistry. *Environmental Science & Technology.* **58**, 22714-22721 (2024).
24. Brown SS, Stutz J. Nighttime radical observations and chemistry. *Chemical Society Reviews.* **41**, 6405-6447 (2012).
25. Wagner NL, *et al.* N_2O_5 uptake coefficients and nocturnal NO_2 removal rates determined from ambient wintertime measurements. *Journal of Geophysical Research: Atmospheres.* **118**, 9331-9350 (2013).
26. Schwartz SE. Mass-Transport Considerations Pertinent to Aqueous Phase Reactions of Gases in Liquid-Water Clouds. In: *Chemistry of Multiphase Atmospheric Systems* (ed Jaeschke W). Springer Berlin Heidelberg (1986).
27. Knipping EM, *et al.* Experiments and Simulations of Ion-Enhanced Interfacial Chemistry on Aqueous NaCl Aerosols. *Science.* **288**, 301-306 (2000).
28. Piatkowski L, Zhang Z, Backus EHG, Bakker HJ, Bonn M. Extreme surface propensity of halide ions in water. *Nature Communications.* **5**, 4083 (2014).
29. Zhang R, *et al.* Evidence on Interfacial Reaction Governing NO_2 Hydrolysis in Deliquesced Aerosol Particles. *Environmental Science & Technology.* **59**, 11708-11719 (2025).
30. Ammann M, *et al.* Heterogeneous production of nitrous acid on soot in polluted air masses. *Nature.* **395**, 157-160 (1998).
31. Kleffmann J, Becker KH, Wiesen P. Heterogeneous NO_2 conversion processes on acid surfaces: possible atmospheric implications. *Atmospheric Environment.* **32**, 2721-2729 (1998).
32. Zhang R, Gen M, Huang D, Li Y, Chan CK. Enhanced Sulfate Production by Nitrate Photolysis in the Presence of Halide Ions in Atmospheric Particles. *Environmental Science & Technology.* **54**, 3831-3839 (2020).
33. Zhang R, Chan CK. Simultaneous formation of sulfate and nitrate via co-uptake of SO_2 and NO_2 by aqueous NaCl droplets: combined effect of nitrate photolysis and chlorine chemistry. *Atmos Chem Phys.* **23**, 6113-6126 (2023).
34. Martin LR, Damschen DE, Judeikis HS. The reactions of nitrogen oxides with SO_2 in aqueous aerosols. *Atmospheric Environment (1967).* **15**, 191-195 (1981).
35. Chang SG, Toossi R, Novakov T. The importance of soot particles and nitrous acid in oxidizing SO_2 in atmospheric aqueous droplets. *Atmospheric Environment (1967).* **15**, 1287-1292 (1981).
36. Xue J, Yuan Z, Griffith SM, Yu X, Lau AKH, Yu JZ. Sulfate Formation Enhanced by a Cocktail of High NO*x*, SO_2, Particulate Matter, and Droplet pH during Haze-Fog Events in Megacities in China: An Observation-Based Modeling Investigation. *Environmental Science & Technology.* **50**, 7325-7334 (2016).
37. Chen H, *et al.* Simultaneous Reduction and Oxidation of NO_2 on Water Microdroplets Provides Previously Unknown Pathways to the Formation of HONO and HNO_3. *Journal of the American Chemical Society.* **147**, 38500-38507 (2025).
38. Ma P, *et al.* Regime-Dependence of Nocturnal Nitrate Formation via N_2O_5 Hydrolysis and Its Implication for Mitigating Nitrate Pollution. *Geophysical Research Letters.* **50**, e2023GL106183 (2023).
39. Zhang Y, *et al.* Double-Edged Role of VOCs Reduction in Nitrate Formation: Insights from Observations during the China International Import Expo 2018. *Environmental Science & Technology.* **57**, 15979-15989 (2023).
40. Yang S, *et al.* The formation and mitigation of nitrate pollution: comparison between urban and suburban environments. *Atmos Chem Phys.* **22**, 4539-4556 (2022).
41. Xie Y, *et al.* Nitrate-dominated $PM_{2.5}$ and elevation of particle pH observed in urban Beijing during the winter of 2017. *Atmos Chem Phys.* **20**, 5019-5033 (2020).
42. Ge S, *et al.* Abundant NH_3 in China Enhances Atmospheric HONO Production by Promoting the Heterogeneous Reaction

of SO_2 with NO_2. *Environmental Science & Technology.* **53**, 14339-14347 (2019).

43. Lu C, Niu S, Tang L, Lv J, Zhao L, Zhu B. Chemical composition of fog water in Nanjing area of China and its related fog microphysics. *Atmospheric Research.* **97**, 47-69 (2010).

44. Zhang S*, et al.* Chemical characteristics of size-resolved fog water at an urban site in Nanjing and the summit of Mt. Lu, East China. *Atmospheric Environment.* **263**, 118667 (2021).

45. Li P, Li X, Yang C, Wang X, Chen J, Collett JL. Fog water chemistry in Shanghai. *Atmospheric Environment.* **45**, 4034-4041 (2011).

46. Liu Y*, et al.* The promotion effect of nitrous acid on aerosol formation in wintertime in Beijing: the possible contribution of traffic-related emissions. *Atmos Chem Phys.* **20**, 13023-13040 (2020).

47. Prather KA*, et al.* Bringing the ocean into the laboratory to probe the chemical complexity of sea spray aerosol. *Proceedings of the National Academy of Sciences.* **110**, 7550-7555 (2013).

48. Collins DB*, et al.* Direct aerosol chemical composition measurements to evaluate the physicochemical differences between controlled sea spray aerosol generation schemes. *Atmos Meas Tech.* **7**, 3667-3683 (2014).

49. Li M, Su H, Li G, Ma N, Pöschl U, Cheng Y. Relative importance of gas uptake on aerosol and ground surfaces characterized by equivalent uptake coefficients. *Atmos Chem Phys.* **19**, 10981-11011 (2019).

50. Li S*, et al.* Contribution of Vehicle Emission and NO_2 Surface Conversion to Nitrous Acid (HONO) in Urban Environments: Implications from Tests in a Tunnel. *Environmental Science & Technology.* **55**, 15616-15624 (2021).

51. Yang C*, et al.* New Insights on the Formation of Nucleation Mode Particles in a Coastal City Based on a Machine Learning Approach. *Environmental Science & Technology.* **58**, 1187-1198 (2024).

52. Hersbach H*, et al.* The ERA5 global reanalysis. *Quarterly Journal of the Royal Meteorological Society.* **146**, 1999-2049 (2020).

53. Fountoukis C, Nenes A. ISORROPIA II: a computationally efficient thermodynamic equilibrium model for K^+; Ca^{2+}; Mg^{2+}; NH_4^+; Na^+; SO_4^{2-}; NO_3^-; Cl^-; H_2O aerosols. *Atmos Chem Phys.* **7**, 4639-4659 (2007).

54. Wolfe GM, Marvin MR, Roberts SJ, Travis KR, Liao J. The Framework for 0-D Atmospheric Modeling (F0AM) v3.1. *Geosci Model Dev.* **9**, 3309-3319 (2016).

55. Yan C*, et al.* Increasing contribution of nighttime nitrogen chemistry to wintertime haze formation in Beijing observed during COVID-19 lockdowns. *Nature Geoscience.* **16**, 975-981 (2023).

56. Lin Z*, et al.* Trends of peroxyacetyl nitrate and its impact on ozone over 2018–2022 in urban atmosphere. *npj Climate and Atmospheric Science.* **7**, 192 (2024).

57. Seinfeld JH, Pandis SN, Noone KJ. Atmospheric Chemistry and Physics: From Air Pollution to Climate Change. *Physics Today.* **51**, 88-90 (1998).

58. Jacob DJ. Chemistry of OH in remote clouds and its role in the production of formic acid and peroxymonosulfate. *Journal of Geophysical Research: Atmospheres.* **91**, 9807-9826 (1986).

59. Gao J*, et al.* Hydrogen peroxide serves as pivotal fountainhead for aerosol aqueous sulfate formation from a global perspective. *Nature Communications.* **15**, 4625 (2024).

60. Boyce SD, Hoffmann MR. Kinetics and mechanism of the formation of hydroxymethanesulfonic acid at low pH. *Journal of Physical Chemistry.* **88**, 4740-4746 (1984).

61. Yu C, Liu T, Chi X, Huang X, Ding A. Ionic Strength Inhibits the Multiphase Reaction Rate between Dissolved SO_2 and HCHO in Aqueous Aerosols: Implications for Sources of Atmospheric Hydroxymethanesulfonate. *Environmental Science & Technology.* **59**, 15900-15906 (2025).

62. Dovrou E, Bates KH, Moch JM, Mickley LJ, Jacob DJ, Keutsch FN. Catalytic role of formaldehyde in particulate matter formation. *Proceedings of the National Academy of Sciences.* **119**, e2113265119 (2022).

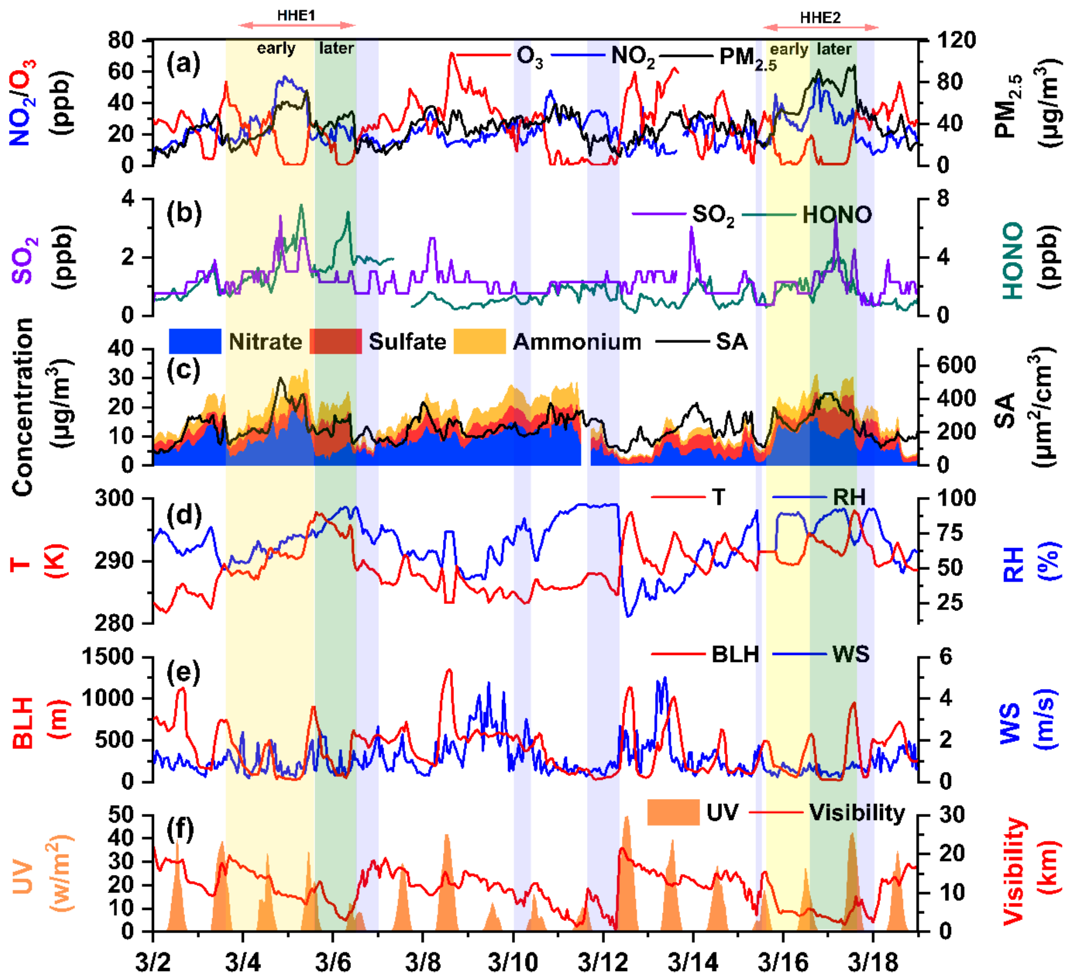

Fig. 1 Chronology of field observations from March 2 to 18, 2024. The figure shows the time series of chemical species and meteorological parameters measured in Xiamen. (**a**) NO_2, O_3 and $PM_{2.5}$ concentrations; (**b**) SO_2 and HONO concentrations; (**c**) concentrations of water-soluble inorganic ions (sulfate, nitrate and ammonium) in $PM_{2.5}$ and aerosol surface area (SA); (**d**) temperature and relative humidity (RH). (**e**) boundary layer height (BLH) and wind speed (WS); (**f**) ultraviolet (UV) radiation and visibility. Two high-humidity events (HHE1 and HHE2) were identified during March 3–6 and March 15–17 during the observation period. The yellow and green shading denote the early stage (ES-HHE) and the later stage of HHEs (LS-HHE), respectively. The ES-HHE was characterized by a rapid increase in NO_3^- concentration, while the LS-HHE was characterized by a rapid increase in SO_4^{2-} concentration. Blue shading indicates rainy periods, while unshaded intervals represent normal periods.

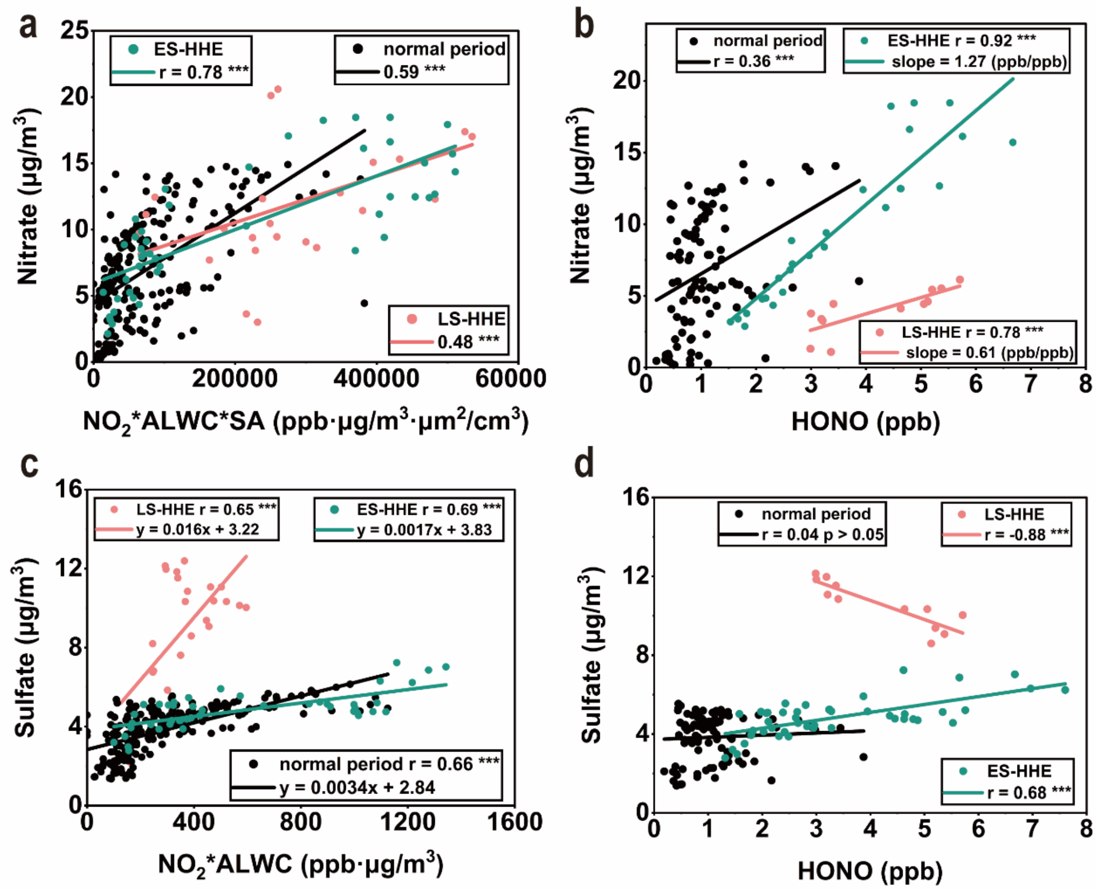

Fig. 2 Observational evidence of potential NO_3^- and SO_4^{2-} formation mechanisms. Relationships between (**a**) $NO_2\times ALWC\times SA$ and NO_3^-, (**b**) observed HONO and NO_3^-, (**c**) $NO_2\times ALWC$ and SO_4^{2-}, (**d**) observed HONO and SO_4^{2-}. Linear regression fits and Pearson correlation coefficients (r) are shown for different periods. The product $NO_2\times ALWC\times SA$ indicates the heterogeneous reaction capability of NO_2, and $NO_2\times ALWC$ indicates its aqueous reaction capacity. Statistical significance is denoted as *** ($p < 0.001$).

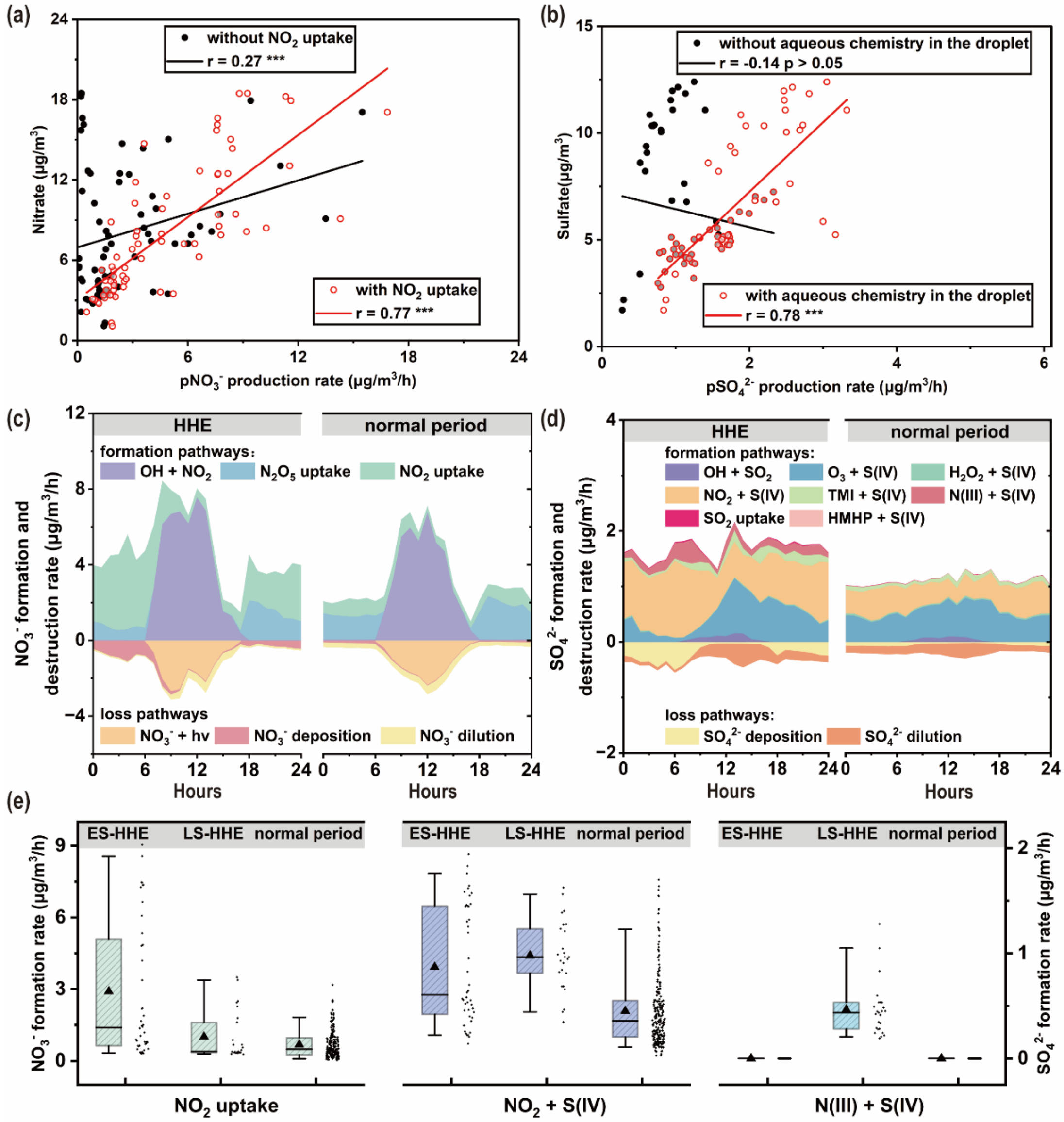

Fig. 3 Quantified results from the multiphase chemical box model. (**a**) Relationship between simulated NO_3^- production rates and observed NO_3^- concentrations during HHE, comparing scenarios with and without heterogeneous NO_2 uptake mechanisms; (**b**) Relationship between simulated SO_4^{2-} production rates and observed SO_4^{2-} concentrations during HHE, comparing scenarios with and without aqueous chemistry in fog droplets; Diurnal variations of NO_3^- budgets (**c**) and SO_4^{2-} budgets (**d**) during HHE period and normal periods; (**e**) Comparison of simulated formation rates via NO_2-driven oxidation pathways including NO_2 uptake, S(IV) oxidation by NO_2(aq), and S(IV) oxidation by N(III) across different periods; Results in panels (c-d) are based on simulations over the entire observation period (Supplementary Figure 5). Boxplots show 25th–75th percentiles with whiskers, black lines, and black triangles representing 5th–95th percentiles, median and mean values, respectively.

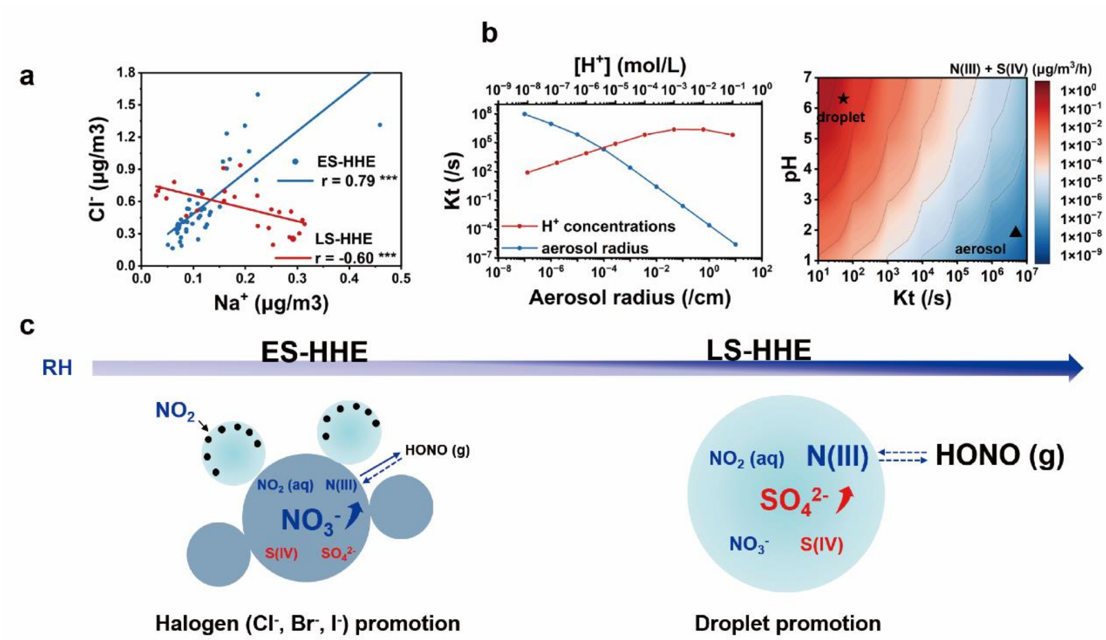

Fig. 4 Schematic of NO_2-driven multiphase oxidation during high-humidity events in southern China. Difference of marine-transported halogen influences between ES-HHE and LS-HHE periods (**a**). Impact of physicochemical properties on S(IV) oxidation rates by N(III) (**b**). Illustration of mechanisms for NO_2-driven multiphase oxidation during high-humidity events (**c**). Panel (a) indicates ES-HHE was influenced by halogen-containing aerosols from marine, while the LS-HHE was increasingly influenced by continental air masses. Panel (b) shows the effects of aerosol radius and H^+ concentration on the calculated mass transfer coefficient ($k_{t,N(III)}$) as well as the combined effects of $k_{t,N(III)}$ and aerosol/droplet pH on simulated S(IV) oxidation rates by N(III). Additionally, the triangle and pentagon symbols in panel (b) represent mean simulated N(III) + S(IV) reaction rates that characterize typical aerosol properties and droplet properties during HHEs, respectively.